

# Lateral quantum confinement effect on monolayer high- $T_c$ superconductors

Guanyang He,<sup>1</sup> Yu Li,<sup>1</sup> Yuxuan Lei,<sup>1,4</sup> Andreas Kreisel,<sup>5</sup> Brian M. Andersen,<sup>5</sup> and Jian Wang<sup>1,2,3,4\*</sup>

<sup>1</sup>*International Center for Quantum Materials, School of Physics, Peking University, Beijing 100871, China*

<sup>2</sup>*Collaborative Innovation Center of Quantum Matter, Beijing 100871, China*

<sup>3</sup>*Hefei National Laboratory, Hefei 230088, China*

<sup>4</sup>*Beijing Academy of Quantum Information Sciences, Beijing 100193, China*

<sup>5</sup>*Niels Bohr Institute, University of Copenhagen, 2100 Copenhagen, Denmark*

(Dated: December 30th, 2023)

Despite decades of research in spatially confined superconducting systems to understand the modification of superconductivity from reduced length scales, the investigation of the quantum confinement effect on high-temperature superconductors remains an outstanding challenge. Here, we report scanning tunneling spectroscopy measurements on laterally confined FeSe monolayers on SrTiO<sub>3</sub> substrates, which are formed by epitaxially growing FeSe films with a coverage less than one unit cell. Comparing to the uniform regions of FeSe monolayers, the peninsula regions at the monolayer boundary exhibit reduced Fermi energy and undiminished superconductivity, leading to a putative crossover from a Bardeen-Cooper-Schrieffer state to a Bose-Einstein condensate state. In isolated FeSe monolayer islands, superconductivity is shown to exist in samples of smaller volume in contrast to conventional superconductors, while the validity of Anderson's criterion remains fulfilled. Our work reveals lateral quantum confinement effects in unconventional superconductors, to enrich the understanding of high-temperature superconductivity in low-dimensional systems.

**Introduction.** When the size of a superconductor goes below or becomes comparable to certain characteristic length scales, such as the superconducting (SC) coherence length  $\xi$ , quantum confinement can modify SC properties and generate novel phenomena. Decades of active research has been fueled by the quantum confinement effect on superconductivity, and especially enriched by the study of two-dimensional (2D) superconductors with thicknesses less than  $\xi$ . Nowadays, 2D superconductors have become an important platform to study quantum phase transitions and other important quantum behavior<sup>1-9</sup>. As the area of 2D superconductors decreases, lateral quantum confinement can also affect the local electronic structure and superconductivity.

Despite extensive research in quantum confinement effects, the lateral quantum confinement in 2D high critical temperature ( $T_c$ ) superconductors remains unexplored. Considering the small  $\xi$  of high- $T_c$  superconductors<sup>10</sup>, it is particularly challenging to

approach these characteristic lengths laterally. In this work, to investigate such quantum confinement by scanning tunneling microscopy/spectroscopy (STM/S), we grew monolayer FeSe on SrTiO<sub>3</sub>(001) (STO) substrate with a coverage less than one unit cell, to generate laterally confined monolayer FeSe films and islands. The 0.55 nm thickness of FeSe monolayers is below its coherence length  $\xi \sim 1.2$  nm. Two kinds of laterally confined FeSe monolayer are studied. The first is FeSe peninsulas near the film boundaries with confined widths around ten nanometers, where the SC gap remains intact, but the Fermi energy ( $E_F$ ) is reduced significantly. Accordingly, the SC pairing strength  $\Delta/E_F$  varies from 0.28 for uniform FeSe monolayers to 0.73 for peninsulas, indicating a putative crossover from the Bardeen-Cooper-Schrieffer (BCS) regime to the Bose Einstein condensation (BEC) regime. The second is isolated monolayer FeSe islands with areas around tens of square nanometer, where a coexistence of Coulomb gap and SC gap is observed. Upon decreasing the size

of the FeSe islands, the SC gap is reduced and eventually disappears. Our findings turn out consistent with the Anderson criterion, i.e. that for small enough superconductors, the electronic energy level spacing destabilizes SC order<sup>11</sup>.

**Methods.** Our experiments are conducted in a molecular beam epitaxy (MBE) - STM combined system (Scienta Omicron, Inc.) with an ultrahigh vacuum of  $1 \times 10^{-10}$  mBar, where the FeSe monolayer is epitaxially grown on Nb-doped SrTiO<sub>3</sub> (001) (wt 0.7%) substrates (STO). STO is thermally annealed in vacuum at 1050 °C for 40 minutes to obtain an atomically flat TiO<sub>2</sub>-terminated surface. The FeSe monolayer is grown by co-evaporating high-purity Fe (99.994%) and Se (99.999%), with the substrate held at 400 °C. Then, the as-grown FeSe film is annealed at 450 °C for 2 hours.

The STS data is measured *in situ* in the STM at 4.2 K by a polycrystalline Pt/Ir tip and standard lock-in technique. The modulation voltage on the tip is 1 mV at 1.769 kHz. The set-up of STS measurements is  $V = 40$  mV,  $I = 2.5$  nA for tunneling spectra, and  $V = 1$  V,  $I = 0.2$  nA for topographic images unless specified otherwise.

**Results and Discussions.** The STM topographic image of our monolayer FeSe grown on the STO terraces is shown in Fig. 1a, and the inset provides the top Se atom arrangement of it. In Fig. 1b, a symmetrized  $dI/dV$  tunneling spectrum is obtained from STS measurements in the central uniform area of monolayer FeSe (see Supplementary for spectra symmetrization), exhibiting prominent coherence peaks and U-shaped SC gaps at 4.2 K. The two-band Dynes model with anisotropic SC gap functions fits the  $dI/dV$  spectrum well to give two gap values  $\Delta_1 = 10.3$  meV and  $\Delta_2 =$

18.1 meV<sup>12</sup>.

Quasiparticle interference (QPI) in the differential conductance mapping  $g(\mathbf{r}, E) = dI/dV(\mathbf{r}, eV)$  provides a powerful tool to analyze electronic states<sup>13-15</sup>. First,  $g(\mathbf{r}, E)$  are obtained on FeSe monolayers. After Fourier transform (FT), the modulus of FT-QPI  $|g(\mathbf{q}, E)|$  as the scattering intensity exhibits three types of ring-like scattering structures, denoted by  $\mathbf{q}_1$ ,  $\mathbf{q}_2$  and  $\mathbf{q}_3$  rings in Fig. 1c;  $\mathbf{q}$  is the momentum transfer of the scattering momenta  $\mathbf{k}$  on the Fermi pockets ( $\mathbf{q} = \mathbf{k}_1 - \mathbf{k}_2$ ). Due to the tunneling-matrix-element effect and the orbital structure of the Fermi pockets, the  $\mathbf{q}_1$  ring exhibits the highest scattering intensity and most complete ring shape<sup>12,16</sup>, therefore is used to extract the band dispersion. Since the elastic scattering from the opposite side of the pocket ( $-\mathbf{k} \leftrightarrow +\mathbf{k}$ ) normally results in the highest intensity at  $\mathbf{q} = 2\mathbf{k}$ <sup>14</sup>, the band dispersion is approximately  $E(\mathbf{k}) = E(\mathbf{q}/2)$ . The energy evolution of the  $\mathbf{q}_1$  ring is resolved from maximum-intensity points in a  $|\mathbf{q}|-E$  plane, corresponding to the dark points on both sides of the  $|\mathbf{q}| = 0$  position in Fig. 1d. Here, as the  $\mathbf{q}_1$  ring corresponds to the scattering within an electron pocket, the ring size shrinks as the energy decreases. The red dashed line in Fig. 1d is a parabolic fitting for the band dispersion (dark points), and  $E_F$  is extracted from the distance between the bottom of the parabola and the Fermi level<sup>15,17</sup>. To present a sharper image, the contributions to the scattering intensity by other electronic pockets inside the parabola are manually subtracted (see Supplementary for QPI analysis). With more QPI measurements in other uniform areas (Fig. S6 and Table S1), an average of  $E_F = 65.3$  meV is obtained, close to results in the literature<sup>17</sup>.

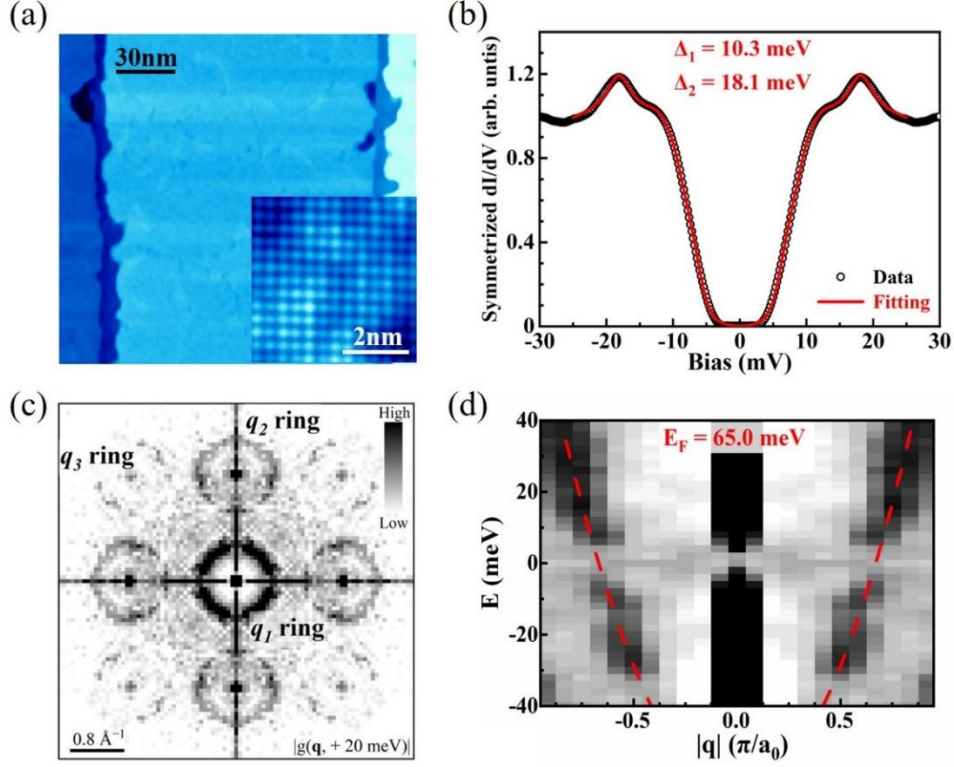


**Fig. 1 STM topography, tunneling spectrum and band dispersion of the uniform area of FeSe monolayers.** (a) Large-scale STM topographic image of the FeSe monolayer grown on STO terraces, where darker colors mean lower heights. The inset is an atomically resolved image showing the topmost Se lattice of FeSe. (b) A typical symmetrized  $dI/dV$  spectrum measured at 4.2 K in the uniform area of a FeSe monolayer. The red curve is the theoretical Dynes fit. (c) Typical FT-QPI pattern of  $|g(\mathbf{q}, E = 20 \text{ meV})|$  after symmetrization, showing three types of ring-like structures denoted by  $\mathbf{q}_1$ ,  $\mathbf{q}_2$  and  $\mathbf{q}_3$  rings. (d) Intensity plot in the  $|\mathbf{q}|-E$  plane, where  $|\mathbf{q}| = 0$  corresponds to the center of (c). The intensity at each energy is plotted versus the radial coordinate near the  $\mathbf{q}_1$  ring position after azimuthal averaging, showing the energy evolution of the  $\mathbf{q}_1$  ring.  $a_0 = 0.38 \text{ nm}$  is the lattice constant of FeSe. The red dashed line is a parabolic fitting for the maximum-intensity points at each energy to find  $E_F$ .

Figure 2a shows a peninsula structure at the boundary of a FeSe monolayer, spatially confined in the width as indicated by the double arrow; the dark area is the STO substrate. In the dashed box region, QPI measurements are performed again to extract the band dispersion (Fig. 2b), and the  $dI/dV$  tunneling spectrum is measured (Fig. 2c). The resolution of  $|\mathbf{q}|$  from a QPI area of  $L \times L$  is  $2\pi/L$ . Considering a minimum value of  $L = 7.8 \text{ nm}$  in Fig. 2a, the  $|\mathbf{q}|$  resolution is around  $0.1 (\pi/a_0)$ , which appears sufficient to reveal the band dispersion in Fig. 2b. By the same method to determine  $E_F$  in the previous paragraph,  $E_F$  in this peninsula appears much smaller than that in the uniform area by nearly 40 meV (from 65.3 to 26.8 meV). The energy band becomes flatter in the peninsulas with a decreased Fermi velocity

$v_F = \frac{1}{\hbar} \frac{\partial E}{\partial k} \approx 2.8 \times 10^4 \text{ m/s}$  (calculated from Fig. 2b), which is smaller than  $v_F \approx 7.1 \times 10^4 \text{ m/s}$  in the uniform area (calculated from Fig. 1d). Meanwhile, the Dynes fitting of SC gaps in Fig. 2c gives  $\Delta_1 = 9.3 \text{ meV}$  and  $\Delta_2 = 19.5 \text{ meV}$ , which barely change from those in the uniform area ( $\Delta_1 = 10.2 \text{ meV}$ ,  $\Delta_2 = 18.1 \text{ meV}$ ), considering the possible gap value fluctuation in monolayer FeSe/STO of around 1.5 meV<sup>18</sup>. Figure 2d-f show the results of another peninsula, which corroborates the reduction of  $E_F$  and the undiminished SC gaps. Similar results from many more peninsulas are exhibited in the supplementary Fig. S8 and S9, and a summarization of all  $\Delta$  and  $E_F$  values is given in Fig. 2g and Table S2. For each point in Fig. 2g, the horizontal error bar represents

the standard deviation of the parabolic fitting for  $E_F$ , and the vertical error bar represents the standard deviation of the Dynes fitting for SC gaps. Moreover, the temperature dependence of the tunneling spectra is measured from 4.2 K to 42 K, and the BCS fitting for  $\Delta_{1,2}(T)$  gives  $T_c \approx 49$  K (see Fig. S7 in Supplementary). Thus,  $T_c$  is nearly unchanged from the uniform area to the peninsulas.

Generally speaking, superconducting  $T_c$  and  $\Delta$  are supposed to decrease sharply in the presence of quantum confinement because of the Anderson criterion<sup>19</sup>. On the other hand, for monolayer FeSe/STO, it is believed that an increased carrier density in FeSe (due to electron doping from STO) can boost superconductivity<sup>20-22</sup>. In our monolayer FeSe peninsulas, the effective mass of the electrons  $m^* = \frac{\hbar^2 |k_F|^2}{2E_F}$  is larger than that in the uniform area because of the reduced  $E_F$  (see Fig. S10b in Supplementary for  $m^*$ ).

Since the carrier density of states is proportional to  $m^*$  for two-dimensional systems, such enlarged  $m^*$  because of quantum confinement could suggest the boosted superconductivity as well. Superconductivity in the unconventional superconductors Al, In, and Sn nano-particles is enhanced with the decrease of sample sizes<sup>23,24</sup>, which is ascribed to phonon softening caused by the small sample size, specifically by structural changes in lattice or contributions from surface phonons<sup>11,25,26</sup>. In our case, the factors related to quantum confinement mentioned above may counteract with each other to a certain extent, so that  $\Delta$  and  $T_c$  remain nearly unchanged in the peninsulas as discussed in the previous paragraph. Moreover, a stronger electron correlation is expected due to the decreased  $v_F$  (larger  $m^*$ ) in the peninsulas, resulting in the BCS-BEC crossover that will be discussed in the next paragraph.

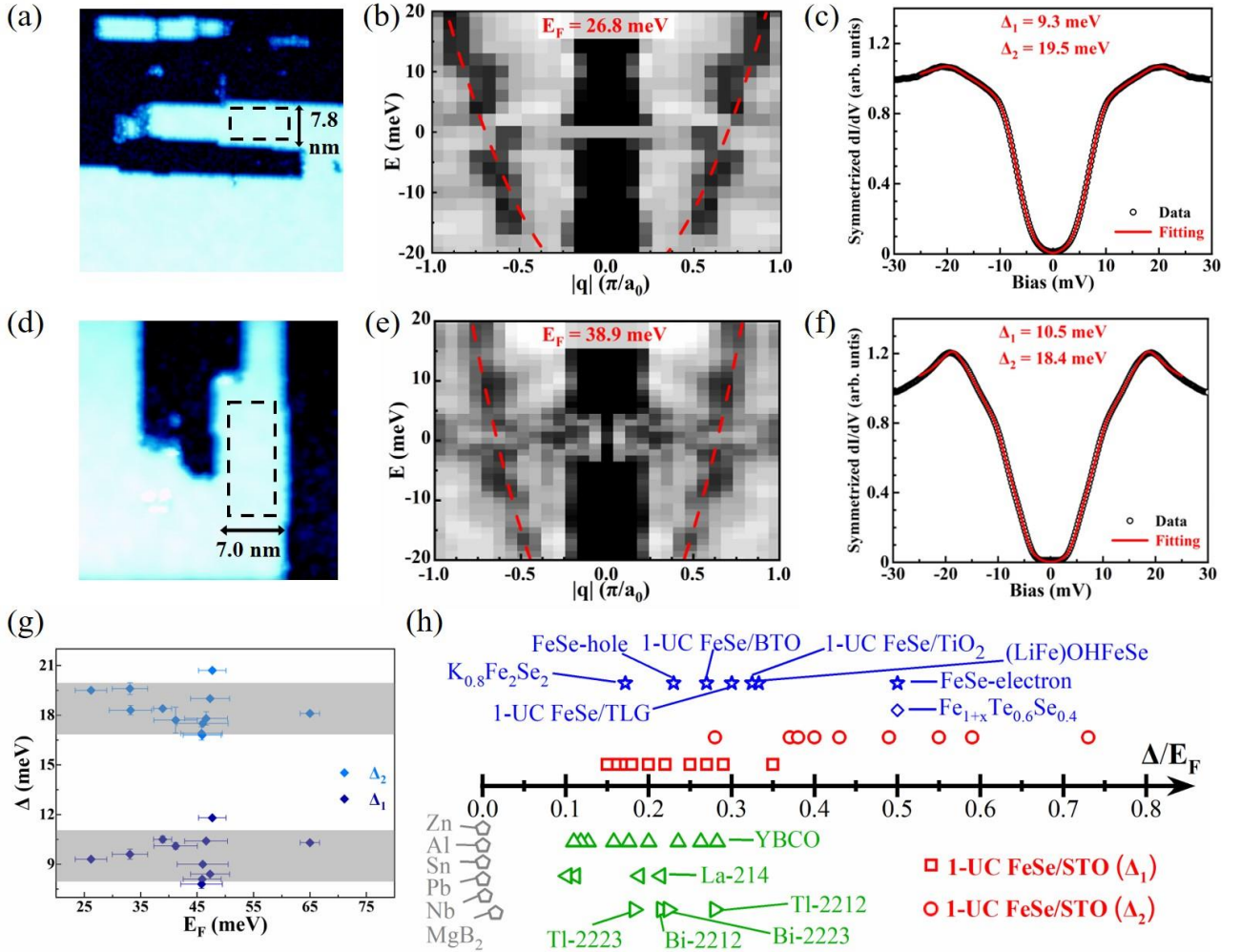


**Fig. 2 STM topographies, band dispersions and tunneling spectra in the peninsulas of FeSe monolayer.** (a) STM topographic image of a peninsula at the monolayer boundary. The dashed box indicates the area of QPI analysis, and the double arrow indicates the peninsula width. (b) Band dispersion extracted from the QPI patterns in the boxed region of (a) by a parabolic fitting. (c) Symmetrized tunneling spectrum measured at the center of the dashed box in (a) with a Dynes fitting. (d-f) Similar results to (a-c) for another peninsula. (g) The summarized results of  $\Delta$  and  $E_F$  from different peninsulas (peninsula widths from 6 to 27 nm). (h) Multiple SC systems in the BCS limit and BCS-BEC crossover regime. Grey pentagons represent the results from conventional superconductors. Green symbols represent cuprates. Blue symbols represent iron-based superconductors. Red symbols represent our results in (g).

The microscopic theory of superconductivity is based on the formation of fermion pairs. With a weak attractive interaction between fermions, they pair in momentum space with a large pair size  $\xi$ , classified as the BCS limit. With a strong attractive interaction, fermions will be bound in pairs tightly in real space; such preformed pairs undergo BEC to the superfluid state afterwards, classified as the BEC limit. These two limits are connected through an intermediate unitary regime called BEC-BCS crossover<sup>27,28</sup>. This crossover is important for understanding strongly correlated electronic systems, attracting attention in cold atoms and condensed matter fields. In cold atom systems, such crossover is realized by tuning the interaction strength between atoms. The interaction strength is specified by the scattering length  $a_s$ , which diverges at the BEC-BCS crossover. Also, the ratio of  $\Delta/E_F$  is around 0.5 as a hallmark of this crossover<sup>29</sup>. In condensed matter systems,  $\Delta/E_F$  is studied in various superconductors as we summarize in Fig. 2h. For conventional superconductors Al, Sn, and Nb,  $\Delta/E_F$  is nearly zero<sup>30</sup>, and for MgB<sub>2</sub> the value of  $\Delta/E_F$  is 0.016<sup>31</sup>, all suggesting BCS limit. On the other hand, BCS-BEC crossover is discussed in high- $T_c$  cuprates due to the quasi-2D nature and strong pairing<sup>32</sup>.  $\Delta/E_F$  values of cuprates are higher than those of conventional superconductors, but mostly lower than 0.3. Specifically, the upward triangles in Fig. 2h refer to YBa<sub>2</sub>Cu<sub>3</sub>O<sub>x</sub>, leftward triangles to La<sub>2-x</sub>Sr<sub>x</sub>CuO<sub>4</sub>, and rightward triangles to Tl<sub>2</sub>Ba<sub>2</sub>Ca<sub>2</sub>Cu<sub>3</sub>O<sub>10</sub>, Bi<sub>2</sub>Sr<sub>2</sub>CaCu<sub>2</sub>O<sub>8</sub>, Bi<sub>2</sub>Sr<sub>2</sub>Ca<sub>2</sub>Cu<sub>3</sub>O<sub>10</sub>, Tl<sub>2</sub>Ba<sub>2</sub>CaCu<sub>2</sub>O<sub>8</sub><sup>33-35</sup>. In iron-based superconductors, the effects of chemical doping have been explored, and  $\Delta/E_F$  of bulk Fe<sub>1+x</sub>Te<sub>0.6</sub>Se<sub>0.4</sub> can be raised from 0.16 to 0.50 by reducing  $x$ <sup>36</sup>. Different substrates have also been used to tune the band edge of

FeSe monolayers; a FeSe monolayer grown on trilayer graphene (TLG) features  $\Delta/E_F = 0.3$ <sup>37</sup>. Bulk FeSe exhibits uniquely tiny hole ( $E_F \sim 10$  meV) and electron pockets ( $E_F \sim 3$  meV) at the Fermi surface<sup>13</sup>, and  $\Delta = 2.3$  or 1.5 meV for the hole or electron band, respectively<sup>38</sup>. Thus  $\Delta/E_F \sim 0.23$  or 0.5 for the hole or electron band of bulk FeSe. In our work, monolayer FeSe/STO has much larger  $T_c$  and yet a larger  $E_F$ , yielding  $\Delta_2/E_F = 0.28$  in the uniform area of our sample; this ratio is dramatically raised to 0.73 due to the lateral quantum confinement of the peninsula area. The BCS-BEC crossover in the peninsula could be pertinent to the enhanced electron correlation discussed in the previous paragraph, as strongly correlated electrons tend to condense into BEC-like pairs<sup>39</sup>. Therefore, monolayer FeSe peninsulas constitute a promising platform to study the BCS-BEC crossover modulation in condensed matter systems. The BEC regime might be considered to associate with pseudo-gap behavior from preformed Cooper pairs<sup>40</sup>, while our peninsulas are in the crossover regime and no evidence of such pseudo-gaps is found as the temperature is raised from 4.2 to 42 K (Fig. S7).

Next, we focus on isolated islands of monolayer FeSe as shown in Fig. 3a, which are more spatially confined comparing to the peninsulas. When the size of a nano-island is small enough, electrons inside the island create a strong Coulomb repulsion preventing the tunneling of an external electron, known as Coulomb blockade. When the applied voltage overcomes the electrostatic energy, external electrons can tunnel into the island one at a time, leading to equidistant conductance peaks in the differential conductance spectrum known as the Coulomb staircase<sup>41</sup>. Figure 3b shows the tunneling spectrum measured on the FeSe



island in Fig. 3a. Except for the gap at the Fermi surface (i.e., zero bias) which will be discussed later, pronounced differential conductance oscillations with nearly equidistant peaks is observed. The peak spacing is labeled by “U” in Fig. 3b. This observed phenomenon is consistent with the scenario of Coulomb staircase peaks, where the voltage interval U is related to the addition energy of an electron to the island.  $U = e/C_1$  depends on the capacitance  $C_1$  between the island and STM tip<sup>42,43</sup>, and the observation of  $U = 14.0$  mV (Fig. 3b) gives  $C_1 = 11.4$  aF. The black dots in Fig. 3c summarize the values of U in FeSe islands of different sizes (see more results in Fig. S11). For each dot, the error bar represents the standard deviation of U from multiple Coulomb staircase peaks measured on one island. These dots follow a linear relation (red dashed line) between U and  $1/S$ , confirming the relationship  $U = e/C_1 \propto 1/S$ , S as the area of monolayer FeSe islands.

The inset of Fig. 3b shows an enlarged view at zero bias, where a gap appears bigger than U and asymmetric about zero bias. The asymmetry about zero bias can be attributed to the residual charge on the island. According to orthodox Coulomb blockade theory<sup>42,43</sup>, the Coulomb blockade gap ( $e/C_2$ ) due to the island-substrate capacitance  $C_2$  is expected to show up at zero bias together with the gap of  $U = e/C_1$ , which is not our case. Our observation of a single gap at zero bias (Fig. 3b) may suggest that  $C_2$  is much larger than  $C_1$  and thus the Coulomb blockade gap ( $e/C_2$ ) is negligible, considering the tiny area of STM tip. Interestingly, the zero-bias gap does not exhibit a monotonous relation with S (the area of monolayer FeSe islands) in Fig. 3d. Since either the gap of  $e/C_1$  or  $e/C_2$  is supposed to be inversely proportional to S<sup>43</sup>, the Coulomb interaction alone cannot explain the observed zero-bias gap. Given that the SC gap shrinks for a decreasing sample volume (proportional to S in our case) near the Anderson limit<sup>19</sup>, the zero-bias gap could be a mixture of U and the SC gap, as the intrinsic energy gap (SC gap) of an isolated system can add to the Coulomb gap in the  $dI/dV$  spectrum<sup>44,45</sup>. We note within a typical capacitively-coupled superconducting island scenario, there is an expected even-odd effect arising from paired vs. unpaired electrons<sup>19</sup>.

Nevertheless, we have only observed weak fluctuations in the addition energy of electrons between even and odd conductance peaks (see Fig. S12 in Supplementary). The absence of a clear even-odd effect for the FeSe islands studied in this work may be related to the reduction of superconductivity in the biased case due to the low critical superfluid density of the islands.

At zero bias voltage (low tunneling current), similar to the addition of U and the SC gap in Sn nanoparticles and Pb islands<sup>46,47</sup>, we can calculate the underlying SC gap  $\Delta$  with the assumption that the enlarged energy gap equals  $U + 2\Delta$ <sup>47</sup>. The calculated  $\Delta$  shown as black dots in Fig. 3e reduces with the decrease of FeSe island volume, where the error bar indicates the standard deviation of U. The red dashed line is a guide to the eye. Such behavior can be expected since small superconductors experience large thermal fluctuations in the order parameter which quenches superconductivity<sup>11,48-50</sup>. Moreover, the Anderson criterion suggests that SC state will completely disappear, when the mean electronic energy level spacing (Kubo gap)  $\delta$  near  $E_F$  exceeds the SC gap<sup>51</sup>. In a system of volume  $V$ ,  $\delta$  is around  $\frac{2\pi^2\hbar^2}{m^*k_F V}$ , where  $k_F$  is the Fermi wave vector and  $m^*$  the effective electron mass<sup>52</sup>. For monolayer FeSe with or without lateral confinement,  $k_F$  is both around  $2.7 \text{ nm}^{-1}$  (Fig. S10a).  $m^*$  is enlarged in the presence of lateral confinement for peninsulas (Fig. S10b), and could be even larger in the case of isolated islands. Thus, by adopting the largest  $m^* = 10.9 m_e$  in Fig. S10b,  $\delta$  vs  $V$  is plotted in Fig. 3e as the blue dashed line. The Anderson limit is estimated by the intersection between two dashed lines in red and blue colors where  $\delta = \Delta$ , giving a critical volume of  $29 \text{ nm}^3$ . In contrast to conventional superconductors with Anderson limits around  $64 \sim 216 \text{ nm}^3$ <sup>11</sup>, superconductivity persists in monolayer FeSe islands down to a smaller volume. The critical volume of  $29 \text{ nm}^3$  is also consistent with the fact that we do not detect any SC gap in islands smaller than  $29 \text{ nm}^3$  (Fig. S11d).

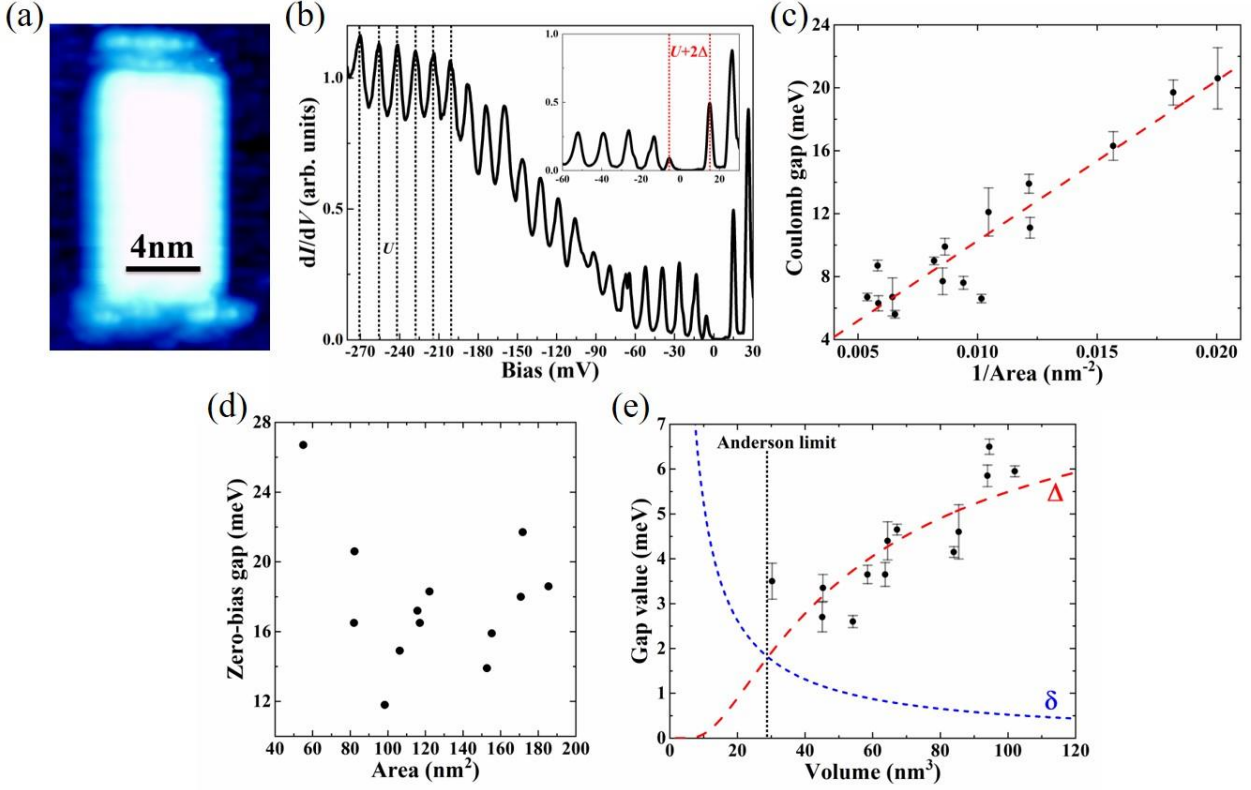


**Fig. 3 Coexistence of Coulomb gap and SC gap in isolated monolayer FeSe islands.** (a) Topographic image of a rectangular monolayer FeSe island on STO substrates. (b) Tunneling spectrum measured on the island in (a). The periodic gap  $U$  away from zero bias is the Coulomb gap. The enlarged gap at zero bias consists of the Coulomb gap  $U$  and SC gap. (c) Coulomb gaps in relation to the reciprocal of the island area, with the dashed line showing a linear fitting. (d) Dependence of the enlarged gap at zero bias on the island area. (e) SC gap value vs the volume of FeSe islands. The red dashed line is a guide to the eye for SC gap  $\Delta$ , and the blue dashed line shows the Kubo gap  $\delta$ . Anderson limit is estimated by the intersection between two dashed lines.

In conclusion, our work reveals how lateral quantum confinement affects the unconventional superconductivity of monolayer FeSe/STO in peninsula structures and isolated islands. In our experiments, lateral quantum confinement brings a clear reduction in  $E_F$ , but nearly undiminished superconductivity in FeSe peninsulas. A potential BCS-BEC crossover is thus detected, indicating a scenario that fermions form pairs before condensation in such low-dimensional high- $T_c$  superconductors. The pairing strength  $\Delta/E_F$  is tuned by lateral quantum confinement from 0.28 to 0.73, suggesting a new method to reach the BCS-BEC crossover regime. For the first time, our work reveals that QPI analysis can be used to study the quantum confinement effect on low-dimensional superconductors. As the lateral confinement becomes

more severe in isolated monolayer FeSe islands, superconductivity is found to be suppressed and coexists with Coulomb blockade effect. The evolution of the SC gap with the volume of monolayer FeSe islands is investigated, where superconductivity eventually disappears near the Anderson limit of  $29 \text{ nm}^3$ . This limit is much smaller than that in conventional superconductors, demonstrating that the Anderson limit is a valid criterion also in unconventional superconductors.

This work was supported by the National Key Research and Development Program of China (Grant No. 2018YFA0305604), the National Natural Science Foundation of China (Grant No. 11888101), the Innovation Program for Quantum Science and Technology (2021ZD0302403).

## References

- <sup>1</sup> YenHsiang Lin, J Nelson, and AM Goldman, Superconductivity of very thin films: The superconductor–insulator transition. *Physica C: Superconductivity and its Applications* **2015**, 514, 130.
- <sup>2</sup> Qingyan Wang, Zhi Li, Wenhao Zhang, Zuocheng Zhang, Jinsong Zhang, Wei Li, Hao Ding, Yunbo Ou, Peng Deng, Kai Chang, Jing Wen, Canli Song, Ke He, JinFeng Jia, Shuaihua Ji, Yayu Wang, Lili Wang, Xi Chen, Xucun Ma, and QiKun Xue, Interface-induced high-temperature superconductivity in single unit-cell FeSe films on SrTiO<sub>3</sub>. *Chinese Physics Letters* **2012**, 29, 037402.
- <sup>3</sup> Aharon Kapitulnik, Steven A Kivelson, and Boris Spivak, Colloquium: anomalous metals: failed superconductors. *Reviews of Modern Physics* **2019**, 91, 011002.
- <sup>4</sup> Ying Xing, HuiMin Zhang, HaiLong Fu, Haiwen Liu, Yi Sun, JunPing Peng, Fa Wang, Xi Lin, XuCun Ma, QiKun Xue, Jian Wang, and Xincheng Xie, Quantum Griffiths singularity of superconductor-metal transition in Ga thin films. *Science* **2015**, 350, 542.
- <sup>5</sup> Nicolas Reyren, Stefan Thiel, AD Caviglia, L Fitting Kourkoutis, German Hammerl, Christoph Richter, Christof W Schneider, Thilo Kopp, A. S Ruetschi, Didier Jaccard, M Gabay, D. A Muller, J. M Triscone, and J Mannhart, Superconducting interfaces between insulating oxides. *Science* **2007**, 317, 1196.
- <sup>6</sup> Chao Yang, Yi Liu, Yang Wang, Liu Feng, Qianmei He, Jian Sun, Yue Tang, Chunchun Wu, Jie Xiong, Wanli Zhang, Xi Lin, Hong Yao, Haiwen Liu, Gustavo Fernandes, Jimmy Xu, James M. Valles JR, Jian Wang, and Yanrong Li, Intermediate bosonic metallic state in the superconductor-insulator transition. *Science* **2019**, 366, 1505.
- <sup>7</sup> G Logvenov, A Gozar, and I Bozovic, High-temperature superconductivity in a single copper-oxygen plane. *Science* **2009**, 326, 699.
- <sup>8</sup> Cheng Chen, Kun Jiang, Yi Zhang, Chaofei Liu, Yi Liu, Ziqiang Wang, and Jian Wang, Atomic line defects and zero-energy end states in monolayer Fe (Te, Se) high-temperature superconductors. *Nature Physics* **2020**, 16, 536.
- <sup>9</sup> Manabu Yamada, Toru Hirahara, and Shuji Hasegawa, Magnetoresistance measurements of a superconducting surface state of In-induced and Pb-induced structures on Si (111). *Physical review letters* **2013**, 110, 237001.
- <sup>10</sup> Shuyuan Zhang, Tong Wei, Jiaqi Guan, Qing Zhu, Wei Qin, Weihua Wang, Jiandi Zhang, EW Plummer, Xuetao Zhu, Zhenyu Zhang, and Jiandong Guo, Enhanced superconducting state in FeSe/SrTiO<sub>3</sub> by a dynamic interfacial polaron mechanism. *Physical review letters* **2019**, 122, 066802.
- <sup>11</sup> Sangita Bose and Pushan Ayyub, A review of finite size effects in quasi-zero dimensional superconductors. *Reports on Progress in Physics* **2014**, 77, 116503.
- <sup>12</sup> Yu Li, Dingyu Shen, Andreas Kreisel, Cheng Chen, Tianheng Wei, Xiaotong Xu, and Jian Wang, Anisotropic Gap Structure and Sign Reversal Symmetry in Monolayer Fe(Se,Te). *Nano Letters* **2022**, (
- <sup>13</sup> Shigeru Kasahara, Tatsuya Watashige, Tetsuo Hanaguri, Yuhki Kohsaka, Takuya Yamashita, Yusuke Shimoyama, Yuta Mizukami, Ryota Endo, Hiroaki Ikeda, Kazushi Aoyama, Taichi Terashima, Shinya Uji, Thomas Wolf, Hilbert von Löhneysen, Takasada Shibauchi, and Yuji Matsuda, Field-induced superconducting phase of FeSe in the BCS-BEC cross-over. *Proceedings of the National Academy of Sciences* **2014**, 111, 16309.
- <sup>14</sup> M. P. Allan, Kyungmin Lee, A. W. Rost, M. H. Fischer, F. Masee, K. Kihou, C. H. Lee, A. Iyo, H. Eisaki, T. M. Chuang, J. C. Davis, and EunAh Kim, Identifying the 'fingerprint' of antiferromagnetic spin fluctuations in iron pnictide superconductors. *Nature Physics* **2015**, 11, 177.



- 15 Dennis Huang, CanLi Song, Tatiana A Webb, Shiang Fang, CuiZu Chang, Jagadeesh S Moodera, Efthimios Kaxiras, and Jennifer E Hoffman, Revealing the empty-state electronic structure of single-unit-cell FeSe/SrTiO<sub>3</sub>. *Physical review letters* **2015**, 115, 017002.
- 16 Zengyi Du, Xiong Yang, Dustin Altenfeld, Qiangqiang Gu, Huan Yang, Ilya Eremin, Peter J Hirschfeld, Igor I. Mazin, Hai Lin, Xiyu Zhu, and HaiHu Wen, Sign reversal of the order parameter in (Li<sub>1-x</sub>Fe<sub>x</sub>)OHFe<sub>1-y</sub>ZnySe. *Nature Physics* **2018**, 14, 134.
- 17 Q. Fan, W. H. Zhang, X. Liu, Y. J. Yan, M. Q. Ren, R. Peng, H. C. Xu, B. P. Xie, J. P. Hu, T. Zhang, and D. L. Feng, Plain s-wave superconductivity in single-layer FeSe on SrTiO<sub>3</sub> probed by scanning tunnelling microscopy. *Nature Physics* **2015**, 11, 946.
- 18 Chaofei Liu, Ziqiao Wang, Shusen Ye, Cheng Chen, Yi Liu, Qingyan Wang, Qiang-Hua Wang, and Jian Wang, Detection of bosonic mode as a signature of magnetic excitation in one-unit-cell FeSe on SrTiO<sub>3</sub>. *Nano letters* **2019**, 19, 3464.
- 19 Sergio Vlaic, Stéphane Pons, Tianzhen Zhang, Alexandre Assouline, Alexandre Zimmers, Christophe David, Guillemain Rodary, Jean. Christophe Girard, Dimitri Roditchev, and Hervé Aubin, Superconducting parity effect across the Anderson limit. *Nature Communications* **2017**, 8, 1.
- 20 Junfeng He, Xu Liu, Wenhao Zhang, Lin Zhao, Defa Liu, Shaolong He, Daixiang Mou, Fangsen Li, Chenjia Tang, Zhi Li, Lili Wang, Yingying Peng, Yan Liu, Chaoyu Chen, Li Yu, Guodong Liu, Xiaoli Dong, Jun Zhang, Chuangtian Chen, Zuyan Xu, Xi Chen, Xucun Ma, Qikun Xue, and X. J. Zhou, Electronic evidence of an insulator–superconductor crossover in single-layer FeSe/SrTiO<sub>3</sub> films. *Proceedings of the National Academy of Sciences* **2014**, 111, 18501.
- 21 WenHao Zhang, Yi Sun, JinSong Zhang, FangSen Li, MingHua Guo, YanFei Zhao, HuiMin Zhang, JunPing Peng, Ying Xing, HuiChao Wang, Takeshi Fujita, Akihiko Hirata, Zhi Li, Hao Ding, Chenjia Tang, Meng Wang, Qingyan Wang, Ke He, Shuaihua Ji, Xi Chen, Junfeng Wang, Zhengcai Xia, Liang Li, Yayu Wang, Jian Wang, Lili Wang, Mingwei Chen, QiKun Xue, and Xucun Ma, Direct observation of high-temperature superconductivity in one-unit-cell FeSe films. *Chinese Physics Letters* **2014**, 31, 017401.
- 22 Chaofei Liu and Jian Wang, Heterostructural one-unit-cell FeSe/SrTiO<sub>3</sub>: from high-temperature superconductivity to topological states. *2D Materials* **2020**, 7, 022006.
- 23 Susumu Matsuo, Hideo Sugiura, and Seiichiro Noguchi, Superconducting transition temperature of aluminum, indium, and lead fine particles. *Journal of Low Temperature Physics* **1974**, 15, 481.
- 24 W. H. Li, C. W. Wang, C. Y. Li, C. K. Hsu, C. C. Yang, and C. M. Wu, Coexistence of ferromagnetism and superconductivity in Sn nanoparticles. *Physical Review B* **2008**, 77, 094508.
- 25 J. M. Dickey and Arthur Paskin, Size and Surface Effects on the Phonon Properties of Small Particles. *Physical Review B* **1970**, 1, 851.
- 26 Sangita Bose, Pratap Raychaudhuri, Rajarshi Banerjee, Parinda Vasa, and Pushan Ayyub, Mechanism of the Size Dependence of the Superconducting Transition of Nanostructured Nb. *Physical Review Letters* **2005**, 95, 147003.
- 27 Yuji Nakagawa, Yuichi Kasahara, Takuya Nomoto, Ryotaro Arita, Tsutomu Nojima, and Yoshihiro Iwasa, Gate-controlled BCS-BEC crossover in a two-dimensional superconductor. *Science* **2021**, 372, 190.
- 28 Qijin Chen, Jelena Stajic, Shina Tan, and Kathryn Levin, BCS–BEC crossover: From high temperature superconductors to ultracold superfluids. *Physics Reports* **2005**, 412, 1.
- 29 Mohit Randeria and Edward Taylor, Crossover from Bardeen-Cooper-Schrieffer to Bose-Einstein condensation and the unitary Fermi gas. *Annu. Rev. Condens. Matter Phys.* **2014**, 5, 209.

- 30 GP Malik, On the Role of Fermi Energy in Determining Properties of Superconductors: a Detailed Comparative Study of Two Elemental Superconductors (Sn and Pb), a Non-cuprate (MgB<sub>2</sub>) and Three Cuprates (YBCO, Bi-2212 and Tl-2212). *Journal of Superconductivity and Novel Magnetism* **2016**, 29, 2755.
- 31 Maria Iavarone, G Karapetrov, AE Koshelev, WK Kwok, GW Crabtree, DG Hinks, WN Kang, Eunmi Choi, Hyun Jung Kim, and HyeongJin Kim, Two-Band Superconductivity in MgB<sub>2</sub>. *Physical review letters* **2002**, 89, 187002.
- 32 Ivan Božović and Jeremy Levy, Pre-formed Cooper pairs in copper oxides and LaAlO<sub>3</sub>—SrTiO<sub>3</sub> heterostructures. *Nature Physics* **2020**, 16, 712.
- 33 Y. J. Uemura, Condensation, excitation, pairing, and superfluid density in high-T<sub>c</sub> superconductors: the magnetic resonance mode as a roton analogue and a possible spin-mediated pairing. *Journal of Physics: Condensed Matter* **2004**, 16, S4515.
- 34 Øystein Fischer, Martin Kugler, Ivan Maggio-Aprile, Christophe Berthod, and Christoph Renner, Scanning tunneling spectroscopy of high-temperature superconductors. *Reviews of Modern Physics* **2007**, 79, 353.
- 35 Shuyuan Zhang, Guangyao Miao, Jiaqi Guan, Xiaofeng Xu, Bing Liu, Fang Yang, Weihua Wang, Xuetao Zhu, and Jiandong Guo, Superconductivity of the FeSe/SrTiO<sub>3</sub> Interface in View of BCS–BEC Crossover\*. *Chinese Physics Letters* **2019**, 36, 107404.
- 36 Shahar Rinott, K. B. Chashka, Amit Ribak, Emile D. L. Rienks, Amina Taleb-Ibrahimi, Patrick Le Fevre, François Bertran, Mohit Randeria, and Amit Kanigel, Tuning across the BCS-BEC crossover in the multiband superconductor Fe<sub>1+y</sub>SexTe<sub>1-x</sub>: An angle-resolved photoemission study. *Science Advances* **3**, e1602372.
- 37 Haicheng Lin, Wantong Huang, Gautam Rai, Yuguo Yin, Lianyi He, Qi-Kun Xue, Stephan Haas, Stefan Kettemann, Xi Chen, and Shuai-Hua Ji, Real-space BCS-BEC crossover in FeSe monolayers. *Physical Review B* **2023**, 107, 104517.
- 38 P. O. Sprau, A. Kostin, A. Kreisel, A. E. Böhmer, V. Taufour, P. C. Canfield, S. Mukherjee, P. J. Hirschfeld, B. M. Andersen, and J. C. Séamus Davis, Discovery of orbital-selective Cooper pairing in FeSe. *Science* **2017**, 357, 75.
- 39 Y Suzuki, K Wakamatsu, J Ibuka, H Oike, T Fujii, K Miyagawa, H Taniguchi, and K Kanoda, Mott-Driven BEC-BCS Crossover in a Doped Spin Liquid Candidate κ-(BEDT–TTF) 4 Hg 2.89 Br 8. *Physical Review X* **2022**, 12, 011016.
- 40 S Kasahara, T Yamashita, A Shi, R Kobayashi, Y Shimoyama, T Watashige, K Ishida, T Terashima, T Wolf, and F Hardy, Giant superconducting fluctuations in the compensated semimetal FeSe at the BCS–BEC crossover. *Nature communications* **2016**, 7, 12843.
- 41 Marc A Kastner, The single-electron transistor. *Reviews of modern physics* **1992**, 64, 849.
- 42 A. E. Hanna and M. Tinkham, Variation of the Coulomb staircase in a two-junction system by fractional electron charge. *Physical Review B* **1991**, 44, 5919.
- 43 I-Po Hong, Christophe Brun, Marina Pivetta, François Patthey, and Wolf-Dieter Schneider, Coulomb blockade phenomena observed in supported metallic nanoislands. *Frontiers in Physics* **2013**, 1, 13.
- 44 Hermann Grabert and Michel H. Devoret, Single Charge Tunneling: Coulomb Blockade Phenomena in Nanostructures. *Springer Science & Business Media* **2013**, (
- 45 Tiancong Zhu, Wei Ruan, Yan-Qi Wang, Hsin-Zon Tsai, Shuopei Wang, Canxun Zhang, Tianye Wang, Franklin Liou, Kenji Watanabe, and Takashi Taniguchi, Imaging gate-tunable Tomonaga–Luttinger liquids in 1H-MoSe<sub>2</sub> mirror twin boundaries. *Nature materials* **2022**, 21, 748.
- 46 Yonghao Yuan, Xintong Wang, Canli Song, Lili Wang, Ke He, Xucun Ma, Hong Yao, Wei Li, and

- Qikun Xue, Observation of Coulomb Gap and Enhanced Superconducting Gap in Nano-Sized Pb Islands Grown on SrTiO<sub>3</sub>\*. *Chinese Physics Letters* **2020**, 37, 017402.
- 47 Jin Qin, Chenxiao Zhao, Bing Xia, Zerui Wang, Yu Liu, Dandan Guan, Shiyong Wang, Yaoyi Li, Hao Zheng, Canhua Liu, and Jinfeng Jia, Coupling of superconductivity and Coulomb blockade in Sn nanoparticles. *Nanotechnology* **2020**, 31, 305708.
- 48 W. P. Halperin, Quantum size effects in metal particles. *Reviews of Modern Physics* **1986**, 58, 533.
- 49 Maciek Zgirski, Karri. Pekka Riikonen, Vladimir Touboltsev, and Konstantin Arutyunov, Size dependent breakdown of superconductivity in ultranarrow nanowires. *Nano letters* **2005**, 5, 1029.
- 50 Sangita Bose, Antonio M. García. García, Miguel M. Ugeda, Juan D. Urbina, Christian H. Michaelis, Ivan Brihuega, and Klaus Kern, Observation of shell effects in superconducting nanoparticles of Sn. *Nature Materials* **2010**, 9, 550.
- 51 Myron Strongin, R. S. Thompson, O. F. Kammerer, and J. E. Crow, Destruction of Superconductivity in Disordered Near-Monolayer Films. *Physical Review B* **1970**, 1, 1078.
- 52 DC Ralph, CT Black, and M Tinkham, Spectroscopic measurements of discrete electronic states in single metal particles. *Physical review letters* **1995**, 74, 3241.
- 53 Zhenyu Wang, Huan Yang, Delong Fang, Bing Shen, Qiang-Hua Wang, Lei Shan, Chenglin Zhang, Pengcheng Dai, and Hai-Hu Wen, Close relationship between superconductivity and the bosonic mode in Ba<sub>0.6</sub>K<sub>0.4</sub>Fe<sub>2</sub>As<sub>2</sub> and Na(Fe<sub>0.975</sub>Co<sub>0.025</sub>)As. *Nature Physics* **2013**, 9, 42.
- 54 Can-Li Song, Yi-Lin Wang, Ye-Ping Jiang, Zhi Li, Lili Wang, Ke He, Xi Chen, Jennifer E Hoffman, Xu-Cun Ma, and Qi-Kun Xue, Imaging the electron-boson coupling in superconducting FeSe films using a scanning tunneling microscope. *Physical Review Letters* **2014**, 112, 057002.
- 55 Fangsen Li, Hao Ding, Chenjia Tang, Junping Peng, Qinghua Zhang, Wenhao Zhang, Guanyu Zhou, Ding Zhang, Can-Li Song, Ke He, Shuaihua Ji, Xi Chen, Lin Gu, Lili Wang, Xu-Cun Ma, and Qi-Kun Xue, Interface-enhanced high-temperature superconductivity in single-unit-cell FeTe<sub>1-x</sub>S<sub>x</sub> films on SrTiO<sub>3</sub>. *Physical Review B* **2015**, 91, 220503.
- 56 Robert C Dynes, Venkatesh Narayanamurti, and JPm Garno, Direct measurement of quasiparticle-lifetime broadening in a strong-coupled superconductor. *Physical Review Letters* **1978**, 41, 1509.
- 57 RC Dynes, JP Garno, GB Hertel, and TP Orlando, Tunneling study of superconductivity near the metal-insulator transition. *Physical Review Letters* **1984**, 53, 2437.
- 58 Zengyi Du, Xiong Yang, Hai Lin, Delong Fang, Guan Du, Jie Xing, Huan Yang, Xiyu Zhu, and Hai-Hu Wen, Scrutinizing the double superconducting gaps and strong coupling pairing in (Li<sub>1-x</sub>Fe<sub>x</sub>)OHFeSe. *Nature communications* **2016**, 7, 10565.
- 59 Yu Li, Dingyu Shen, Andreas Kreisel, Cheng Chen, Tianheng Wei, Xiaotong Xu, and Jian Wang, Anisotropic gap structure and sign reversal symmetry in monolayer Fe (Se, Te). *Nano Letters* **2022**, 23, 140.
- 60 MJ Lawler, K Fujita, Jinhwan Lee, AR Schmidt, Y Kohsaka, Chung Koo Kim, H Eisaki, S Uchida, JC Davis, and JP Sethna, Intra-unit-cell electronic nematicity of the high-T<sub>c</sub> copper-oxide pseudogap states. *Nature* **2010**, 466, 347.
- 61 Q Fan, WH Zhang, X Liu, YJ Yan, MQ Ren, R Peng, HC Xu, BP Xie, JP Hu, T Zhang, and D.L. Feng, Plain s-wave superconductivity in single-layer FeSe on SrTiO<sub>3</sub> probed by scanning tunnelling microscopy. *Nature Physics* **2015**, 11, 946.
- 62 Dennis Huang, Can-Li Song, Tatiana A Webb, Shiang Fang, Cui-Zu Chang, Jagadeesh S

Moodera, Efthimios Kaxiras, and Jennifer E Hoffman, Revealing the empty-state electronic structure of single-unit-cell FeSe/SrTiO<sub>3</sub>.

*Physical review letters* **2015**, 115, 017002.

## Supplementary Information for

### Lateral quantum confinement effect on monolayer high- $T_c$ superconductors

Guanyang He,<sup>1</sup> Yu Li,<sup>1</sup> Yuxuan Lei,<sup>1,4</sup> Andreas Kreisel,<sup>5</sup> Brian M. Andersen,<sup>5</sup> and Jian Wang<sup>1,2,3,4\*</sup>

<sup>1</sup>*International Center for Quantum Materials, School of Physics, Peking University, Beijing 100871, China*

<sup>2</sup>*Collaborative Innovation Center of Quantum Matter, Beijing 100871, China*

<sup>3</sup>*Hefei National Laboratory, Hefei 230088, China*

<sup>4</sup>*Beijing Academy of Quantum Information Sciences, Beijing 100193, China*

<sup>5</sup>*Niels Bohr Institute, University of Copenhagen, 2100 Copenhagen, Denmark*

#### CONTENTS

STS data processing

Dynes Fitting and BCS Fitting for STS spectra

Quasiparticle Interference Measurements and Band Extraction

Fig. S1. Data process of the tunneling spectra.

Fig. S2. Data process of the FT-QPI patten measured from the uniform area of monolayer FeSe.

Fig. S3. Data process of the band extraction measured from the uniform area of monolayer FeSe.

Fig. S4. Data process of the FT-QPI patten measured from the FeSe peninsula.

Fig. S5. Data process of the band extraction measured from the FeSe peninsula.

Fig. S6. Band dispersions in uniform area of monolayer FeSe.

Fig. S7. Temperature-dependent tunneling spectra in uniform area of monolayer FeSe.

Fig. S8, S9. Topographies, band dispersions from QPI and tunneling spectra in peninsulas of monolayer FeSe.

Fig. S10.  $E_F$  in relation to the Fermi momentum  $|\mathbf{k}_F|$  and the effective mass  $m^*$ .

Fig. S11. Topographies and tunneling spectra for monolayer FeSe islands.

Fig. S12. Possible signatures of the even-odd effect in monolayer FeSe islands.

Table S1.  $E_F$  and  $\Delta_{1,2}/E_F$  values in the uniform area of monolayer FeSe.

Table S2.  $E_F$  and  $\Delta_{1,2}/E_F$  values in FeSe peninsulas.

Table S3.  $\chi^2$  value for different fittings in Fig. S8, S9.

#### STS data processing

Originating from the band edge effect<sup>53</sup>, the tunneling spectrum can be asymmetric with a higher density of states at positive bias voltages than at negative bias voltages. To eliminate such irrelevant effect, our raw STS spectrum (Fig. S1a) is normalized by dividing it by its asymmetric background (Fig. S1b), and the background curve is acquired by a cubic fitting to the raw spectrum in the voltage range away from the Fermi level (25 ~ 40 mV). This data processing method is previously used in the literature<sup>18,54,55</sup>. After the normalization, the particle-hole symmetrization (Fig. S1c) is performed in the next step by averaging all  $dI/dV$  values at  $-V$  and  $+V$  for each  $|V|$ , to give the symmetrized  $dI/dV$  spectra shown in the main text.

## Dynes Fitting and BCS Fitting for STS spectra

The symmetrized spectrum is fitted by the summation of two Dynes functions ( $\frac{dI_1}{dV}$  and  $\frac{dI_2}{dV}$ ) with different weights ( $w$ ):<sup>56,57</sup>

$$G = \left[ w \frac{dI_1}{dV} + (1 - w) \frac{dI_2}{dV} \right]$$

where the Dynes function with anisotropic  $s_{\pm}$ -wave gap structure is given by<sup>58,59</sup>

$$\frac{dI_{1,2}}{dV} = N(E_F) \frac{1}{2\pi} \frac{1}{k_B T} \int_{-\infty}^{+\infty} dE \int_0^{2\pi} d\theta \operatorname{Re} \left[ \frac{|E - i\Gamma_{1,2}|}{\sqrt{(E - i\Gamma_{1,2})^2 - \Delta_{1,2}(\theta)^2}} \right] \cosh^{-2} \frac{E + eV}{2k_B T}$$

$$\Delta_{1,2}(\theta) = \Delta_{1,2}^{max} [1 - p_{1,2}(1 - \cos 4\theta)]$$

In the fitting parameters,  $N(E_F)$  represents the density of states at  $E_F$ ;  $\Gamma$  is the scattering rate stemming from finite-lifetime effects of the quasiparticles at the gap edge [5,6]. Our STS spectra give  $\Gamma \approx 2$  meV at 4.2 K, which is reasonable compared to our large superconducting gaps up to 18 meV.  $p$  is the degree of anisotropy, which should be below 0.5 for nodeless superconducting gaps. Our STS spectra give  $p \approx 0.3$  at 4.2 K, indicating a noticeable gap anisotropy.  $\Delta_{1,2}^{max}$  represents the superconducting gap size, corresponding to the  $\Delta_1$  and  $\Delta_2$  discussed in the main text. For temperature-dependent tunneling spectra,  $\Delta_1$  and  $\Delta_2$  in the main text extracted by the Dynes fittings are further fitted by the BCS gap function to give  $T_c$ :

$$\Delta(T) = \Delta_0 \tanh \left( \frac{\pi}{2} \sqrt{\frac{T_c}{T} - 1} \right)$$

## Quasiparticle Interference Measurements and Band Extraction.

After the differential conductance mapping  $g(\mathbf{r}, E)$  at different energies ( $E$ ) is measured on the uniform area of monolayer FeSe (center of Fig. 1a), Fig. S2 exemplifies the data processing to obtain a sharp FT-QPI pattern. We use Lawler-Fujita Algorithm to correct the distortion of  $g(\mathbf{r}, E)$ <sup>60</sup>. Such correction is firstly performed on the topographic image simultaneously measured with  $g(\mathbf{r}, E)$ , where the best correction parameters are found that eliminate all distortions in the known lattice structure of FeSe. Fig. S2a and S2b show the topographic image and the corresponding FT pattern respectively, which exhibit the non-orthogonality of the  $x$ - $y$  axes and noticeable noise around the Bragg spots. After Lawler-Fujita correction, the topography (Fig. S2c) and the corresponding FT pattern (Fig. S2d) become a strictly tetragonal lattice. Then, the correction parameters for the topography are used in the following Lawler-Fujita correction for  $g(\mathbf{r}, E)$ . The initial  $g(\mathbf{q}, E)$  (Fig. S2e) from the FT of  $g(\mathbf{r}, E)$  is mirror symmetrized and four-fold rotational ( $C_4$ ) symmetrized (Fig. S2f), in order to increase the signal-to-noise ratio. These symmetrization methods are commonly used for the FT-QPI data processing in 1-UC FeSe<sup>61,62</sup>. Next, we use the  $g(\mathbf{q}, 0 \text{ meV})$  to normalize  $g(\mathbf{q}, E \neq 0 \text{ meV})$  in Fig. S2f, to suppress the intensity of tiny scattering vectors around the center (Fig. S2g). Note that this normalization is similar to a Gaussian core subtraction (Fig. S2h), while the latter requires manually inputting the parameters of Gaussian core.

After the above process to obtain Fig. S2g, we take line-cuts of  $|g(\mathbf{q}, E)|$  along  $\theta = 22.5^\circ$  and plot the intensity in a  $|\mathbf{q}|$ - $E$  plane (Fig. S3b), which clearly reveals the electron band structure. We also perform the azimuthal averaging (19 line-cuts evenly spaced between  $0^\circ \sim 45^\circ$ ) to further increase the signal-to-noise ratio (Fig. S3c). As for line-cuts from the initial  $|g(\mathbf{q}, E)|$  without symmetrization or normalization (Fig. S3a), the trend of the band dispersion can be roughly resolved but with poor signal-to-noise ratio. The same data process to obtain Fig. S3c is exhibited in the



results of the peninsula region on monolayer FeSe (Fig. S4 and S5), and used in all results of the main text.

Finally, the band dispersion is obtained from the maximum-intensity points in a  $|\mathbf{q}|$ - $E$  plane, with a parabolic fitting:

$$E = -E_F + \frac{\hbar^2}{2m^*} \cdot |\mathbf{k}|^2, |\mathbf{k}| = |\mathbf{q}|/2$$

$E_F$  is the Fermi energy and  $m^*$  is the effective mass. The band dispersion is fitted with both  $m^*$  and  $E_F$  as free parameters, to extract the  $E_F$  values shown in Fig. 2g, Table. S1, and Table. S2.

In addition, we have also tried to fix  $m^* = 4m_e$  (the  $m^*$  value in Fig. S10b for the uniform area of FeSe monolayer) with only  $E_F$  as free fitting parameters. This  $m^*$  is close to the value we deduce ( $\sim 4.26 m_e$ ) from the reference <sup>61</sup>. Fittings with fixed  $m^*$ /free  $m^*$  parameter are both shown in Fig. S8, S9 by blue/red parabolic curves, where the maximum-intensity points in the  $|\mathbf{q}|$ - $E$  plane are denoted by white circles. The goodness of each fitting is determined by the  $\chi^2$  value (Pearson's chi-square test) summarized in Table. S3, where the fittings with free  $m^*$  parameters appear to be better than those with fixed  $m^*$ , suggesting that  $m^*$  differs between the FeSe peninsula and the uniform area.

Pearson's chi-square is calculated by  $\chi^2 = \sum_i \frac{(E_i - E_{i0})^2}{E_{i0} + 50}$ , where  $E_i$  is the energy of the maximum-intensity point (y-axis coordinate of each white circle in Fig. S8b) and  $E_{i0}$  is the energy on the parabolic curve at the  $|\mathbf{q}|$  value corresponding to  $E_i$ . The addition of 50 meV in the denominator is just to get rid of negative value in the summation of  $\chi^2$ .

## Supplementary Figures and Tables

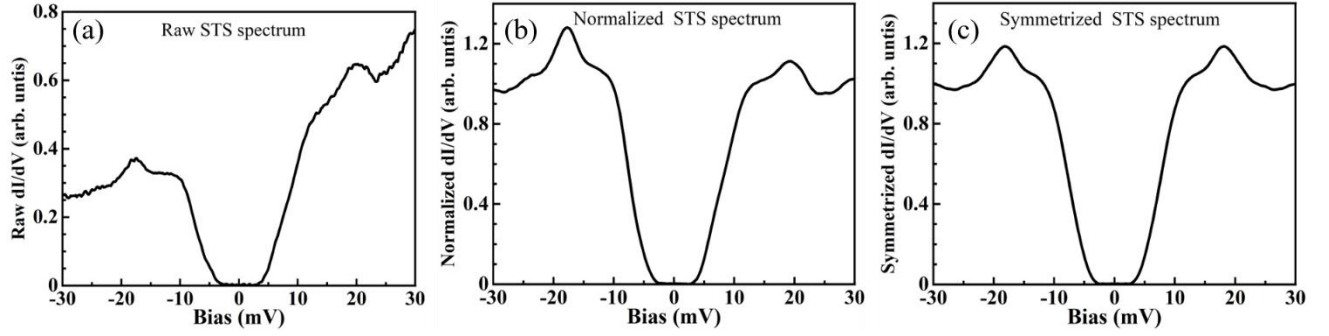


**Fig. S1** One typical example of STS data processing, showing (a) the raw STS data, (b) STS after normalization, (c) STS after normalization and symmetrization.

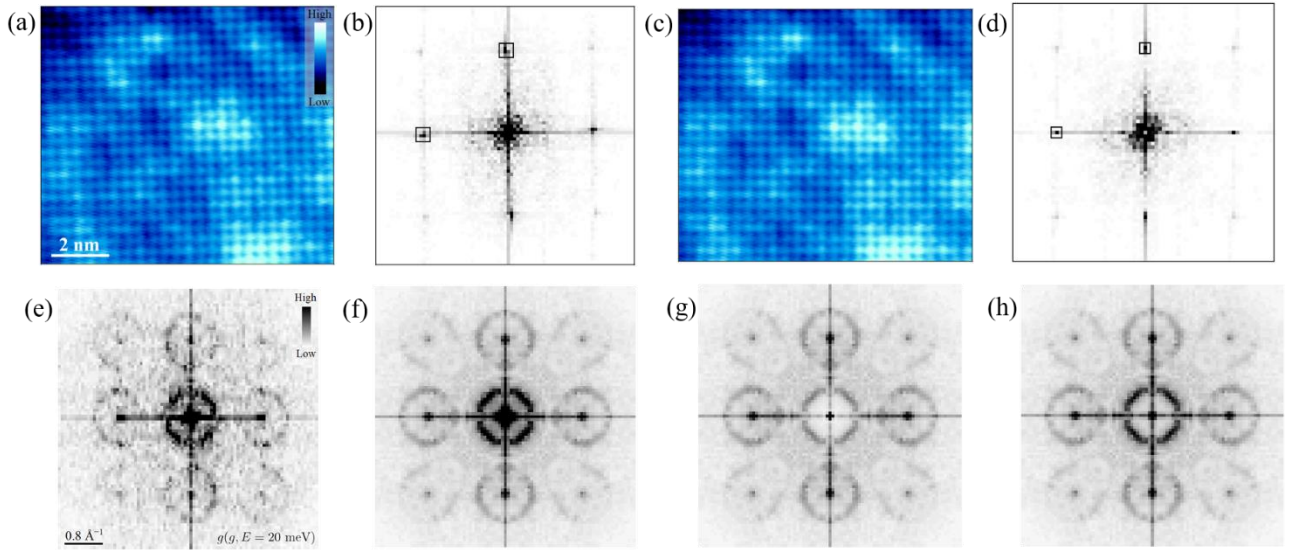


**Fig. S2** FT-QPI pattern measured in the uniform area of FeSe monolayer. (a)-(b) Topographic images before the Lawler-Fujita correction and the corresponding FT pattern. (c)-(d) Topographic images after the Lawler-Fujita correction and the FT pattern. (e)  $|g(\mathbf{q}, E = 20 \text{ meV})|$  as the FT of the Lawler-Fujita corrected differential conductance mapping  $g(\mathbf{r}, E = 20 \text{ meV})$ . (f) Mirror symmetrized and  $C_4$  symmetrized  $|g(\mathbf{q}, E = 20 \text{ meV})|$ . (g)  $|g(\mathbf{q}, E = 20 \text{ meV})|$  normalized by  $|g(\mathbf{q}, E = 0 \text{ meV})|$ . (h)  $|g(\mathbf{q}, E = 20 \text{ meV})|$  with a Gaussian core subtraction.

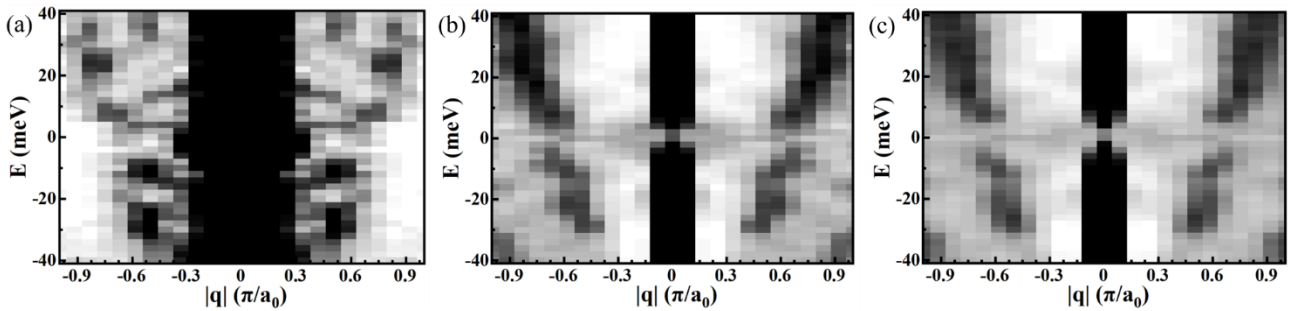


**Fig. S3** Band extraction from the uniform area of FeSe monolayer. (a) Line cuts along  $\theta = 22.5^\circ$  of initial  $|g(\mathbf{q}, E)|$ . (b) Line cuts along  $\theta = 22.5^\circ$  of symmetrized and normalized  $|g(\mathbf{q}, E)|$ . (c) Azimuthally averaged line cuts of symmetrized and normalized  $|g(\mathbf{q}, E)|$ .

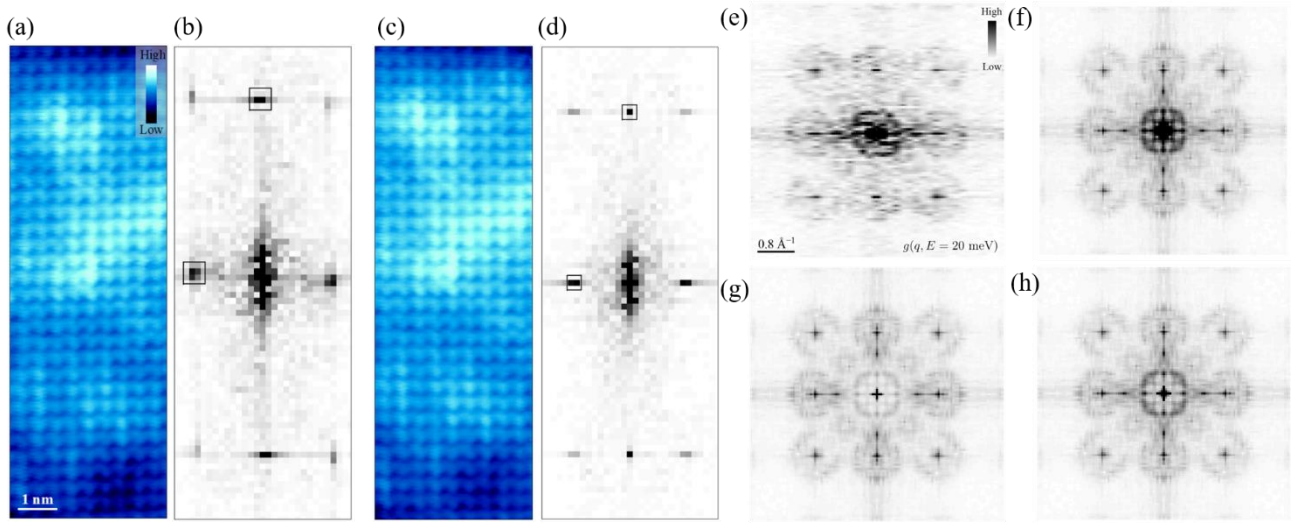


**Fig. S4** FT-QPI pattern measured in the FeSe peninsula. The data process is the same as that in the uniform area of FeSe monolayer (Fig. S2).

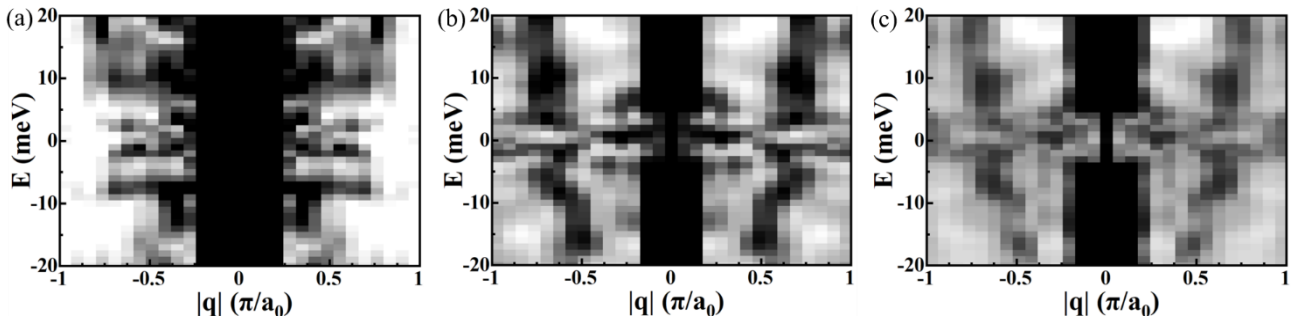


**Fig. S5** Band extraction measured in the FeSe peninsula. The data process is the same as that shown in Fig. S3.

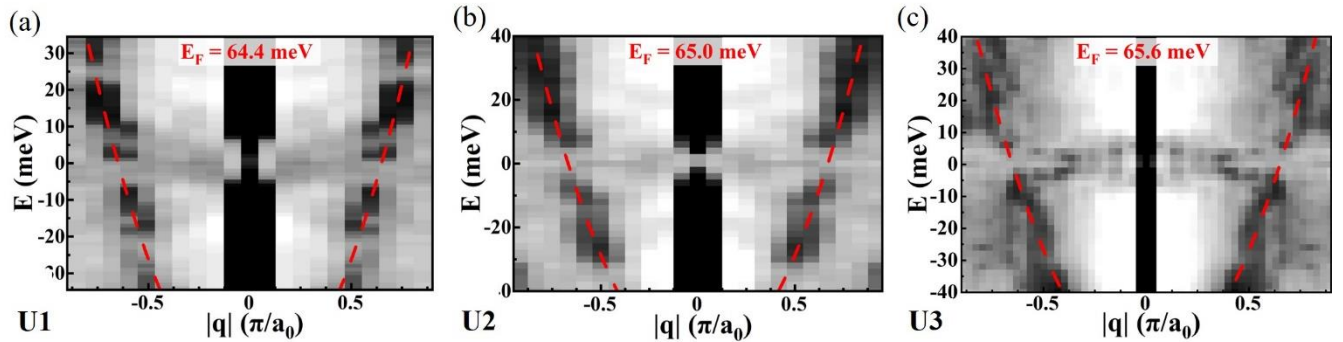


**Fig. S6** Band dispersions obtained from FT-QPI in uniform area (labeled as U1-U5) in the monolayer FeSe. The red dashed curve is the parabolic fitting to obtain  $E_F$ . U3 is shown as Figure 1(d) in the main text.

**Table S1**  $E_F$  and  $\Delta_{1,2}/E_F$  values in the uniform area of monolayer FeSe.

	U1	U2	U3
$E_F$ (meV)	64.4	65.0	65.6
$\Delta_1/E_F$	0.16	0.16	0.15
$\Delta_2/E_F$	0.28	0.28	0.28

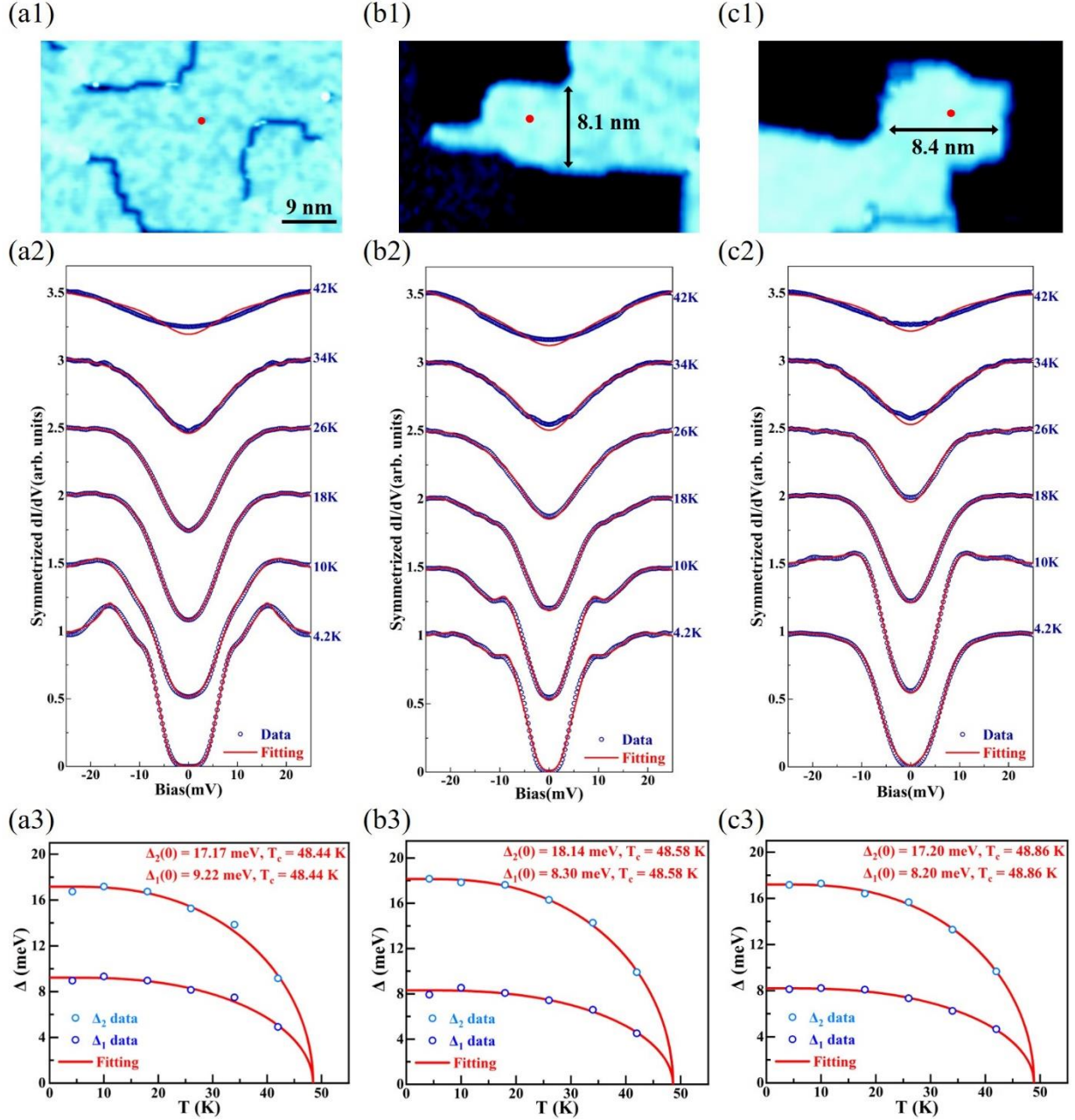


**Fig. S7** (a1) STM topographic image of a central uniform area in the monolayer FeSe, where the red dots denote the location of STS measurements. (a2) Temperature-dependent tunneling spectra (blue dots) with double-band anisotropic Dynes fittings (red curves). The spectra are vertically offset for clarity. (a3) BCS fittings (red curves) of  $\Delta_{1,2}(T)$  values (blue dots) to obtained  $T_c$ . (b1-b3) Similar images and results to (a1-a3), but from a FeSe peninsula at the film boundary. (c1-c3) Images and results from another peninsula.



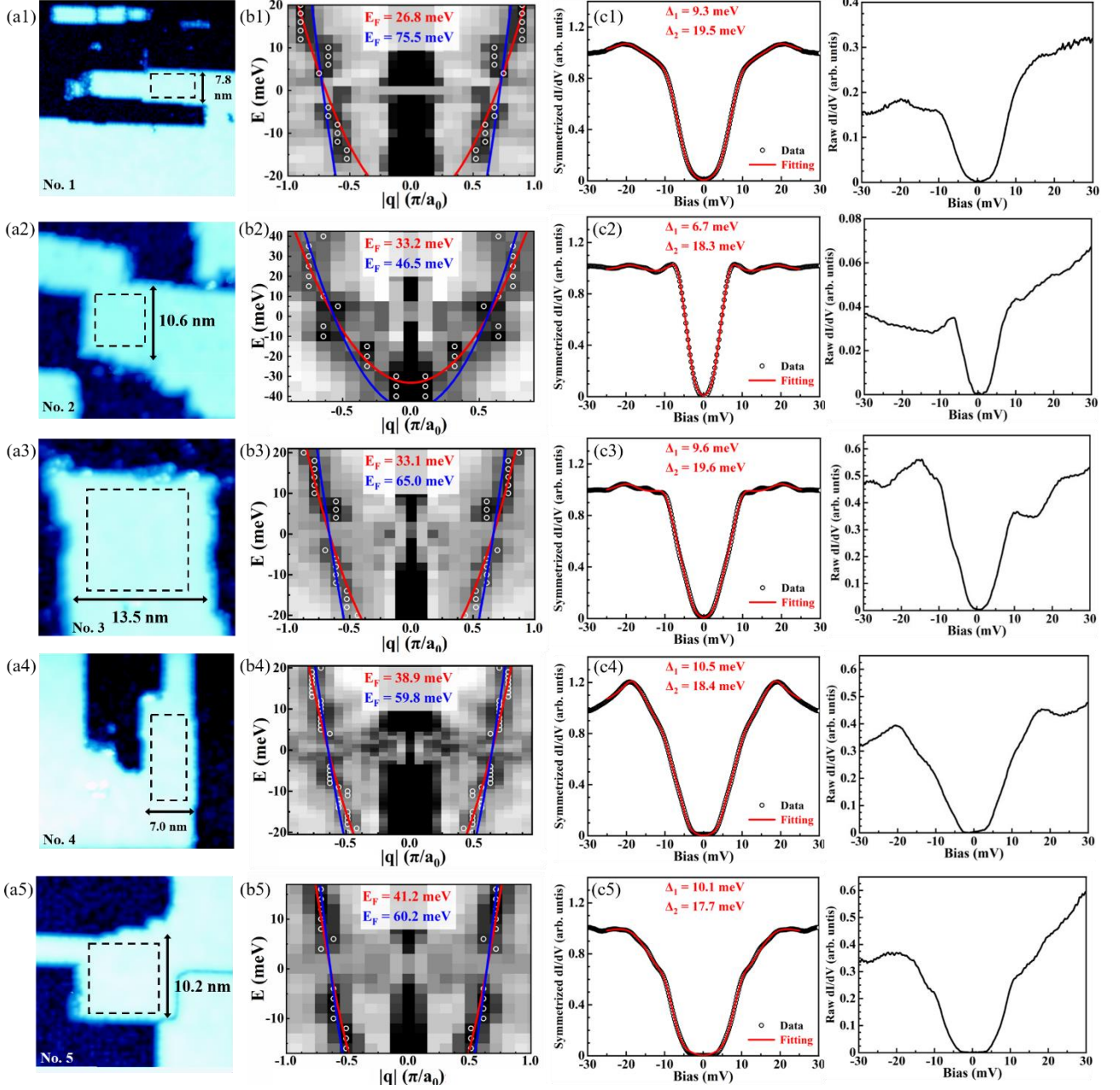


**Fig. S8** (a) STM topographies, (b) Band dispersions from QPI measurements,  $E_F$  values are found by fittings with free  $m^*$  parameter (red parabola) and fixed  $m^* = 4m_e$  (blue parabola) (c) Tunneling spectra in peninsulas at the boundary of monolayer FeSe/STO, with the raw  $dI/dV$  data before normalization and symmetrization shown on the right. (a1) and (a4) correspond to Figure 2(a) and 2(d) in the main text.

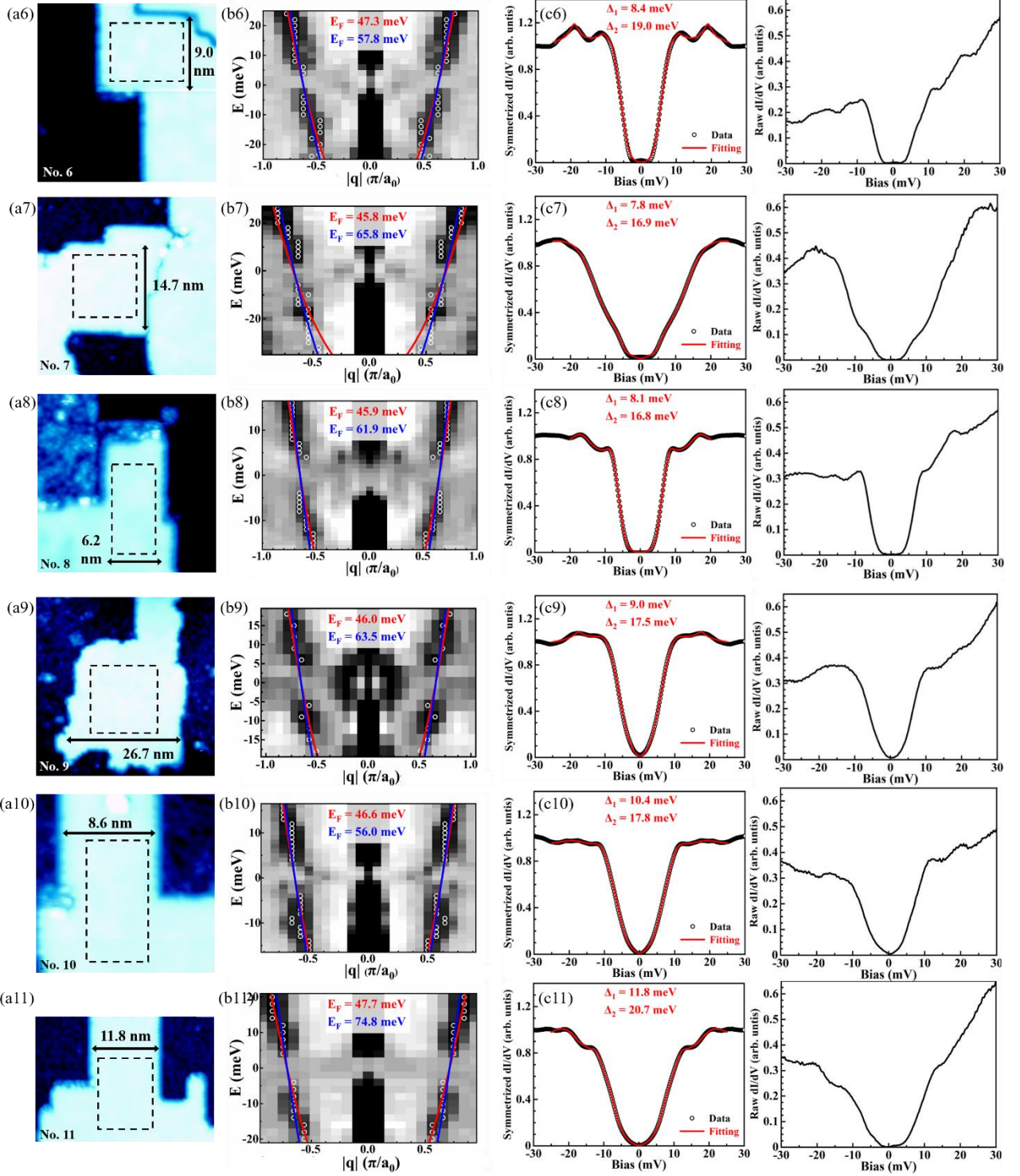


**Fig. S9** Results following Fig. S8. (a) STM topographies, (b) Band dispersions from QPI measurements and (c) tunneling spectra in other peninsulas at the boundary of monolayer FeSe/STO.



**Table S2** All results of  $E_F$  and  $\Delta_{1,2}/E_F$  values in FeSe peninsulas.

No.	1	2	3	4	5	6	7	8	9	10	11
$E_F$ (meV)	26.8	33.2	33.1	38.9	41.2	47.3	45.8	45.9	46.0	446.6	47.7
$\Delta_1/E_F$	0.35	0.20	0.29	0.27	0.25	0.18	0.17	0.18	0.20	0.22	0.25
$\Delta_2/E_F$	0.73	0.55	0.59	0.47	0.43	0.40	0.37	0.37	0.38	0.38	0.43

**Table S3**  $\chi^2$  value for each fitting in Fig. S8, S9.

No.	1	2	3	4	5	6	7	8	9	10	11
$\chi^2$ of fixed $m^*$ fittings	135.2	125.2	70.9	61.0	13.5	29.7	65.0	21.2	8.9	15.3	27.5
$\chi^2$ of free $m^*$ fittings	8.9	37.0	13.4	11.2	5.3	19.4	56.1	12.2	4.1	13.2	4.3

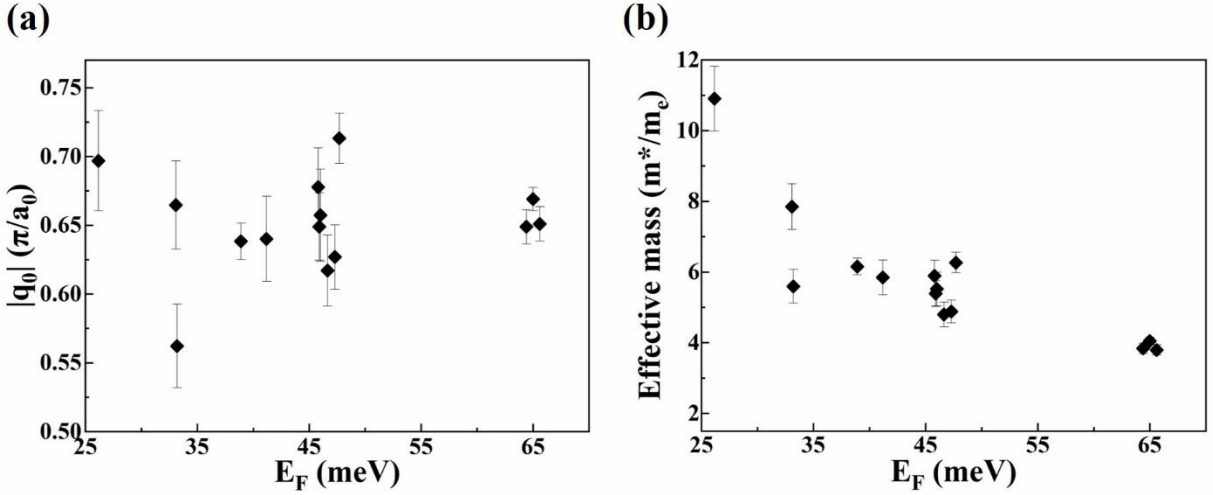


**Fig. S10** (a)  $E_F$  in relation with the Fermi momentum of the band ( $|k_F| = |q_0|/2$ ) (b)  $E_F$  in relation with the effective mass  $m^*$ , in the unit of the electron mass  $m_e$ . Data come from the parabolic fittings for band dispersions in Fig. S6, S8 and S9, and error bars from the parameter uncertainty given by the fitting. Smaller  $E_F$  values correspond to FeSe regions with more lateral confinements such as peninsulas, while larger  $E_F$  values correspond to the uniform region.

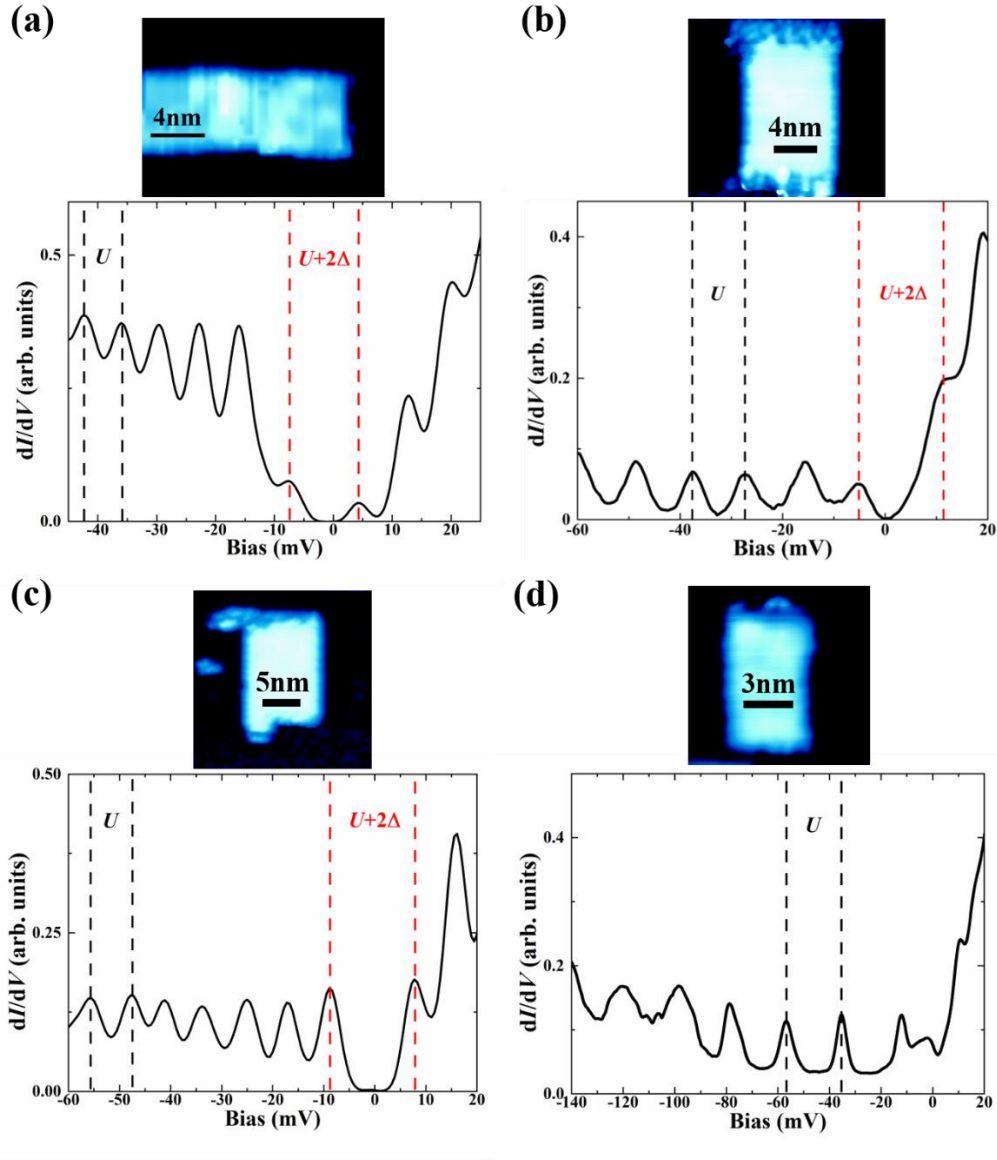


**Fig. S11** Typical topographic images and corresponding tunneling spectra for various monolayer FeSe islands with different volume ( $V$ ). (a)  $V = 54.1 \text{ nm}^2$ ,  $U = 6.6 \text{ meV}$ . (b)  $V = 45.1 \text{ nm}^2$ ,  $U = 11.1 \text{ meV}$ . (c)  $V = 64.4 \text{ nm}^2$ ,  $U = 7.7 \text{ meV}$ . (d)  $V = 23.9 \text{ nm}^2$ ,  $U = 21.0 \text{ meV}$ . The superconducting gap is absent in this island with the volume smaller than the Anderson limit.

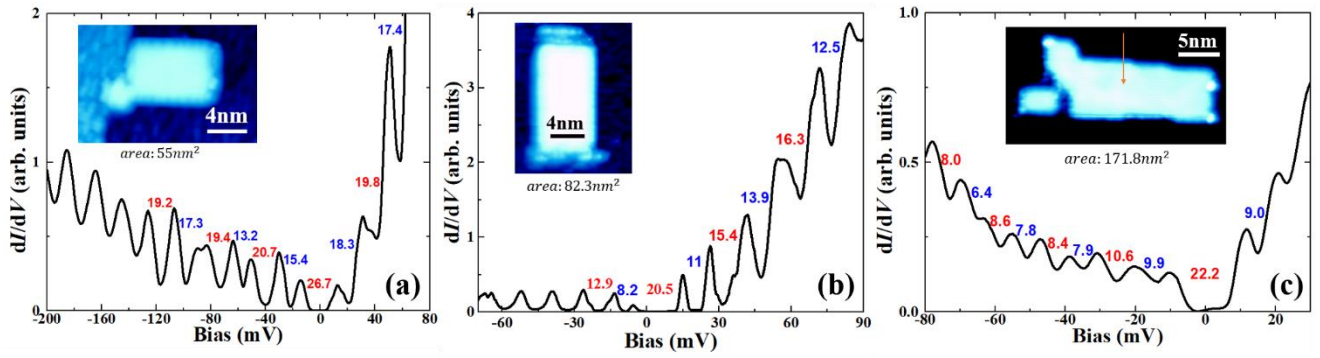


**Fig. S12** Topographic images and corresponding tunneling spectra for three monolayer FeSe islands with possible signatures of the even-odd effect. In the spectra, the number between every two conductance peaks indicates the distance between the peaks. Numbers in red (blue) are larger (smaller) than their neighboring blue (red) numbers, and these two colors alternate.

## References for the Supplementary

- 1 Zhenyu Wang, Huan Yang, Delong Fang, Bing Shen, Qiang-Hua Wang, Lei Shan, Chenglin Zhang, Pengcheng Dai, and Hai-Hu Wen, Close relationship between superconductivity and the bosonic mode in  $\text{Ba}_{0.6}\text{K}_{0.4}\text{Fe}_2\text{As}_2$  and  $\text{Na}_{0.975}\text{Co}_{0.025}\text{As}$ . *Nature Physics*. 9, 42 (2013).
- 2 Can-Li Song, Yi-Lin Wang, Ye-Ping Jiang, Zhi Li, Lili Wang, Ke He, Xi Chen, Jennifer E Hoffman, Xu-Cun Ma, and Qi-Kun Xue, Imaging the electron-boson coupling in superconducting FeSe films using a scanning tunneling microscope. *Physical Review Letters*. 112, 057002 (2014).
- 3 Fangsen Li, Hao Ding, Chenjia Tang, Junping Peng, Qinghua Zhang, Wenhao Zhang, Guanyu Zhou, Ding Zhang, Can-Li Song, Ke He, Shuaihua Ji, Xi Chen, Lin Gu, Lili Wang, Xu-Cun Ma, and Qi-Kun Xue, Interface-enhanced high-temperature superconductivity in single-unit-cell  $\text{Fe}_{1-x}\text{S}_x$  films on  $\text{SrTiO}_3$ . *Physical Review B*. 91, 220503 (2015).
- 4 Chaofei Liu, Ziqiao Wang, Shusen Ye, Cheng Chen, Yi Liu, Qingyan Wang, Qiang-Hua Wang, and Jian Wang, Detection of bosonic mode as a signature of magnetic excitation in one-unit-cell FeSe on  $\text{SrTiO}_3$ . *Nano letters*. 19, 3464 (2019).
- 5 Robert C Dynes, Venkatesh Narayanamurti, and J Pm Garno, Direct measurement of quasiparticle-lifetime broadening in a strong-coupled superconductor. *Physical Review Letters*. 41, 1509 (1978).
- 6 RC Dynes, JP Garno, GB Hertel, and TP Orlando, Tunneling study of superconductivity near the metal-insulator transition. *Physical Review Letters*. 53, 2437 (1984).
- 7 Zengyi Du, Xiong Yang, Hai Lin, Delong Fang, Guan Du, Jie Xing, Huan Yang, Xiyu Zhu, and Hai-Hu Wen, Scrutinizing the double superconducting gaps and strong coupling pairing in  $(\text{Li}_{1-x}\text{Fe}_x)\text{OHFeSe}$ . *Nature communications*. 7, 10565 (2016).
- 8 Yu Li, Dingyu Shen, Andreas Kreisel, Cheng Chen, Tianheng Wei, Xiaotong Xu, and Jian Wang, Anisotropic gap structure and sign reversal symmetry in monolayer Fe (Se, Te). *Nano Letters*. 23, 140 (2022).
- 9 MJ Lawler, K Fujita, Jinhwan Lee, AR Schmidt, Y Kohsaka, Chung Koo Kim, H Eisaki, S Uchida, JC Davis, and JP Sethna, Intra-unit-cell electronic nematicity of the high- $T_c$  copper-oxide pseudogap states. *Nature*. 466, 347 (2010).
- 10 Q Fan, WH Zhang, X Liu, YJ Yan, MQ Ren, R Peng, HC Xu, BP Xie, JP Hu, T Zhang, and D.L. Feng, Plain s-wave superconductivity in single-layer FeSe on  $\text{SrTiO}_3$  probed by scanning tunnelling microscopy. *Nature Physics*. 11, 946 (2015).
- 11 Dennis Huang, Can-Li Song, Tatiana A Webb, Shiang Fang, Cui-Zu Chang, Jagadeesh S Moodera, Efthimios Kaxiras, and Jennifer E Hoffman, Revealing the empty-state electronic structure of single-unit-cell FeSe/ $\text{SrTiO}_3$ . *Physical review letters*. 115, 017002 (2015).